JOURNAL OF PROPULSION AND POWER
Vol. 18, No. 2, March–April 2002

Numerical Simulation of Side Loads in an Ideal Truncated Nozzle

Sébastien Deck* and Philippe Guillen†
ONERA, F-92322 Châtillon, France

The side loads induced by unsymmetrical and unsteady separation of the flow taking place in the nozzle extension during launch are a very important limiting factor for the performance of a rocket engine. The onset of such loads is not yet a fully understood phenomenon because only a limited amount of experimental data is available due to test difficulties. A numerical study of the three-dimensional overexpanded nozzle flow during stationary operations has been undertaken to try to understand the origin of this phenomenon. The flow separation in an truncated ideal contoured nozzle is investigated together with the resulting side loads. Comparisons with experimental data are given. The numerical simulation relies on the resolution of the three-dimensional unsteady Reynolds-averaged Navier–Stokes equations. An algebraic turbulence model based on Baldwin-Lomax and Goldberg's backflow correction has been implemented in a three-zone formulation adapted to the flow topology of interest. The main features of the flowfield, side-loads mean value, and the separation point location are well estimated. With regard to the separation point location, the proposed method gives better results than the most commonly used semi-empirical criteria. Unsteady characteristics of the flowfield are presented.

Nomenclature

E	=	total energy, $\mathrm{m}^{-2}\cdot\mathrm{s}^{-2}$
F_c	=	convection flux
F_d	=	diffusive flux
$F(t)$	=	side-load norm, $\sqrt{[F_y^2(t)+F_z^2(t)]}$, N
$F_{y,z}(t)$	=	side-load components on y, z
$\bar{\bar{I}}$	=	identity matrix tensor
i, j, k	=	indices of cell ijk
ijk, l	=	interface l of cell ijk
M	=	Mach number
$n, n+1$	=	discrete times, corresponding t and $t+\Delta t$, s
P	=	pressure, Pa
Pr, Pr_t	=	Prandtl and turbulent Prandtl numbers
T	=	temperature, K
$\boldsymbol{W}$	=	conservative variable vector
x, y, z	=	physical Cartesian coordinate axes, m
γ	=	ratio of specific heats
$\theta(t)$	=	angle between the side force and Ox axis, rad
κ, κ_t	=	laminar and turbulent thermal conductivities, $\mathrm{kg}\cdot\mathrm{m}^{-1}\cdot\mathrm{s}^{-3}\cdot\mathrm{K}^{-1}$
μ, μ_t	=	laminar and eddy viscosities, $\mathrm{kg}\cdot\mathrm{m}^{-1}\cdot\mathrm{s}^{-1}$
ρ	=	density, $\mathrm{kg}\cdot\mathrm{m}^{-3}$
τ, τ_r	=	viscous stresses, Pa, and Reynolds tensors, Pa

Subscripts

a	=	ambient
b	=	backflow edge
c	=	chamber
t	=	throat (geometry)
v	=	viscous sublayer edge
w	=	wall

Introduction

IN today's advanced launchers, the nozzle of the first-stage rocket engine has to operate from sea-level atmospheric conditions to low ambient pressure environments at high altitudes. The performance of the propulsion system is high in vacuum owing to its design. However, at the very beginning of the flight, the wall pressure level required for an adapted attached flow can be much lower than the ambient pressure. This leads to a flow separation in the nozzle extension. Because of its fluctuating and three-dimensional characteristics, which can result in strong lateral forces and might damage the nozzle structure, this separation is undesired. The most well known of these dynamic loads are the so-called side loads. Different empirical models have been developed to predict side loads. A brief review for their evaluation is given in Ref. 1. Nevertheless, the phenomenon is not fully understood and different possible physical origins have been identified. As a matter of fact, the performance increase of the next generation sea-level nozzles will be strongly dependent on the side-load reduction capabilities.

Experimental side-load measurements are difficult to implement. Hence, numerical approaches remain very promising for the treatment of nonadapted flowfields in rocket nozzles. Indeed in recent years, there has been considerable interest[2–5] in numerical approaches of startup and shutdown processes in thrust optimized nozzles. The possible transition of flowfield separation pattern from free-shock separation to restricted-shock separation, and vice versa, has been invoked as an important side-load source factor.[6–9] The internal shock seems to have a major influence on the separation pattern. Nevertheless, side loads are also observed[10] in an truncated ideal contoured nozzle (without internal shock) during stationary operations with separated flow inside the nozzle.

A three zone algebraic turbulence model adapted to this specific flow topology has been developed, and unsteady three-dimensional turbulent computations have been carried out to try to get a better understanding of the origin of side loads that occur in an truncated ideal contoured nozzle during stationary operation. Because of the experimental low-frequency characteristics[10] of the fluctuating side loads, 10–100 Hz, the attempt to use an unsteady Reynolds-averaged Navier–Stokes approach is legitimate. The two main objectives of this study are 1) the accurate prediction of the separation point location and 2) the comparison between unsteady numerical results and the available experimental data.

Numerical Method

Governing Equations

The governing equations are the Navier–Stokes equations. For turbulent flows, a Reynolds-averaged form is used, where the conservative variables are mass averaged and represent the mean flow contributions:

Received 23 July 2000; revision received 11 April 2001; accepted for publication 1 September 2001.

*Ph.D. Student, ONERA, Applied Aerodynamics Department, Centre National d'Etudes Spatiales.
†Engineer, Applied Aerodynamics Department.

$$\frac{\partial \boldsymbol{W}}{\partial t} + \mathrm{div}(F_c) = \mathrm{div}(F_d) \tag{1}$$

with

$$\boldsymbol{W} = {}^t(\rho, \rho \boldsymbol{V}, \rho E)$$

$$F_c = {}^t[\rho \boldsymbol{V}, \rho(\boldsymbol{V} \otimes \boldsymbol{V}) + p\bar{\bar{1}}, \rho E \boldsymbol{V} + p\boldsymbol{V}]$$

$$F_d = {}^t[0, \bar{\bar{\tau}} + \bar{\bar{\tau}}_r, (\bar{\bar{\tau}} + \bar{\bar{\tau}}_r) \cdot \boldsymbol{V} - (q + \boldsymbol{q}_t)] \tag{2}$$

The preceding system is formulated in an absolute frame.

Turbulence contribution to these averaged equations is reduced to the Reynolds tensor $\bar{\bar{\tau}}_r$ and to the turbulent heat transfer $\boldsymbol{q}_t$.

Assuming the air as an ideal gas, the state equation relates the static pressure P to the conservative variables:

$$P = (\gamma - 1)[\rho E - (\rho \boldsymbol{V})^2 / 2\rho] \tag{3}$$

For a Newtonian fluid, shear stresses are related to mean velocity gradients. Apparent turbulent stresses are also related to mean velocity gradients, following Boussinesq's assumption,

$$\bar{\bar{\tau}} + \bar{\bar{\tau}}_r = (\mu + \mu_t)\left[-\tfrac{2}{3}(\mathrm{div}\, \boldsymbol{V})\bar{\bar{1}} + (\mathrm{grad}\, \boldsymbol{V} + {}^t\mathrm{grad}\, \boldsymbol{V})\right] \tag{4}$$

Sutherland's law is used to account for the dependence of laminar viscosity on temperature:

$$\mu(T) = \mu_0 \left(\frac{T}{T_0}\right)^{\frac{3}{2}} \cdot \frac{T_0 + 110.4}{T + 110.4} \tag{5}$$

with $T_0 = 273.16$ K and $\mu_0 = 1.711.10^{-5}\ \mathrm{kg \cdot m^{-1} \cdot s^{-1}}$.

Considering a finite volume Ω, its surface S with an exterior normal $\boldsymbol{n}$, the integration of local equations (1) leads to the following integral form :

$$\frac{\delta}{\delta t}\left(\int_\Omega \boldsymbol{W}\, \mathrm{d}\Omega\right) + \int_S [F_c \cdot \boldsymbol{n}]\, \mathrm{d}S = \int_S F_d \cdot \boldsymbol{n}\, \mathrm{d}S \tag{6}$$

Numerical Algorithm

The numerical method is based on a finite volume approach [Eq. (6)] and on a cell centered discretization. The computational domain is divided by block; each block is composed of structured hexahedral cells.

Time discretization is based on second-order accurate Gear's[11] formulation of the fully implicit scheme:

$$\frac{\frac{3}{2}\boldsymbol{W}_{ijk}^{n+1} - 2\boldsymbol{W}_{ijk}^{n} + \frac{1}{2}\boldsymbol{W}_{ijk}^{n-1}}{\Delta t} \cdot \bar{\Omega}_{ijk} + \left[\sum_{l=1}^{6} (\boldsymbol{F}_c - \boldsymbol{F}_d)_{ijk,l}\right]^{n+1} = 0 \tag{7}$$

where ijk are the grid indices and l one of the six interfaces of the hexahedral rigid cell Ω_{ijk}, and where the superscripts $n-1$, n, and $n+1$ refer to the time evaluation. The numerical boundary conditions are adiabatic no-slip wall condition and nonreflecting far-field condition. They are imposed by ensuring adequate fluxes at boundary interfaces. Further details of the numerical method may be found in Ref. 12.

Turbulence Modeling

When the Boussinesq hypothesis is assumed, turbulence modeling is reduced to the evaluation of an eddy viscosity μ_t. Algebraic eddy-viscosity models still represent a common choice for compressible Navier–Stokes computations thanks to their minimal CPU and memory requirements, which is particularly important for three-dimensional unsteady computations.

Several two-layer algebraic turbulence models (such as Cebeci and Smith) require the determination of the boundary-layer thickness and edge velocity, which proves to be rather difficult to implement for complex flow topologies. Visbal and Knight,[13] for instance, found the Baldwin–Lomax[14] formulation unsuitable for separated supersonic interaction due to the unphysical streamwise variation of the computed length scale in the vicinity of separation. In addition, the flow of interest in our study involves a large separated area from the nozzle wall and complex shock patterns. To model adequately its turbulent behaviour, an implementation of Goldberg's backflow model[15] has been introduced.

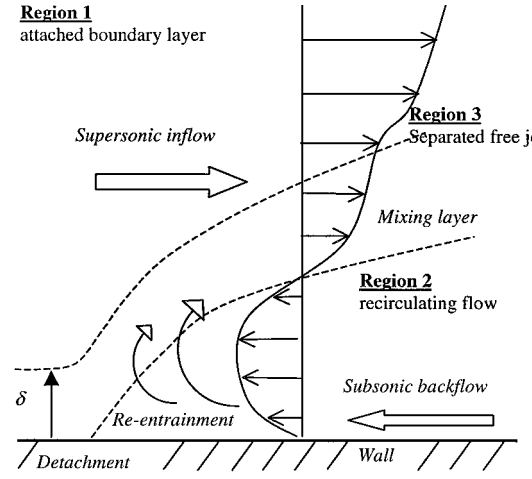

Fig. 1 Schematic of two-dimensional turbulent boundary-layer separation.

More precisely, the overall turbulent model developed here, distinguishes three zones in the flowfield (Fig. 1)

Region 1

The Baldwin–Lomax[14] turbulence model is a two-layer algebraic eddy-viscosity model patterned after that of Cebeci and Smith.[16] A brief description of the model is given here because some adaptations of the original model are performed.

The eddy viscosity is given by

$$\mu_t = \begin{cases} \mu_{ti} & \text{for} \quad y \le y_c \text{ (inner region)} \\ \mu_{te} & \text{for} \quad y > y_c \text{ (outer region)} \end{cases} \tag{8}$$

where y_c is the closest distance to the wall at which the eddy-viscosity values from inner and outer regions are identical.

Inner Region

The eddy viscosity is expressed as

$$\mu_{ti} = \bar{\rho} \|\tilde{\boldsymbol{\Omega}}\| l^2 \tag{9}$$

In case of a three-dimensional flow, $\|\tilde{\boldsymbol{\Omega}}\|$ is chosen as the norm of the vorticity,

$$\|\tilde{\boldsymbol{\Omega}}\| = \sqrt{\left(\frac{\partial u}{\partial y} - \frac{\partial v}{\partial x}\right)^2 + \left(\frac{\partial v}{\partial z} - \frac{\partial w}{\partial y}\right)^2 + \left(\frac{\partial w}{\partial x} - \frac{\partial u}{\partial z}\right)^2} \tag{10}$$

The mixing length l is a correction of the Prandtl mixing length using Van Driest's damping function[17] to reach asymptotic behavior at the wall:

$$l = \chi y [1 - \exp(-y^+ / \tilde{A}^+)] \sqrt{\tau^+} \tag{11}$$

The dimensionless distance y^+, which is a Reynolds number based on the friction velocity u_τ, is given as

$$y^+ = \left(\sqrt{\rho_w |\tau_w|} \big/ \mu_w\right) y = (y u_\tau / \nu_w) \tag{12}$$

The near-wall treatment has been improved to account for the total shear stress being no more constant near the wall in presence

of pressure gradient. The inner layer has also been modified by the shear-stress square root:

$$\tau^+ = 1 + p^+ y^+ \tag{13}$$

where

$$p^+ = \frac{\nu^e}{\rho_w u_\tau^2}\frac{\mathrm{d}P}{\mathrm{d}x} \tag{14}$$

On a flat plate, $A^+ = u_\tau A/\nu$ is constant and equal to 26. To take into account the pressure gradient, A^+ has been modified[18] as follows:

$$\tilde{A}^+ = A^+ \Big/ \sqrt{1 + 44p^+} \tag{15}$$

The constants are von Kármán's $\chi = 0.41$ and Van Driest's[17] damping $A^+ = 26$.

Outer Region

The eddy viscosity is chosen as

$$\mu_{te} = \bar{\rho} k C_{cp} F_w F_{\mathrm{Kleb}}(y) \tag{16}$$

The Clauser parameter k is assigned to be constant and equal to 0.0168 and C_{cp} equal to 1.6. Turbulence decrease in the outer region is taken into account by the Klebanoff intermittence factor:

$$F_{\mathrm{Kleb}}(y) = \left\{1 + 5.5[C_{\mathrm{Kleb}}(y/y_{\max})]^6\right\}^{-1} \tag{17}$$

with $C_{\mathrm{Kleb}} = 0.3$. Turbulence scales F_w are evaluated considering Baldwin's[14] function maximum,

$$F_{\mathrm{Bald}}(y) = y\|\tilde{\Omega}\| \tag{18}$$

with

$$F_w = y_{\max} F_{\mathrm{Bald}_{\max}} \tag{19}$$

The difficulty is to select the right maximum because the Baldwin function usually presents several: a first one near the wall at about $y^+ \approx 10$, the right second maximum characteristic of the boundary-layer edge, and sometimes a vortex maximum outside the boundary layer for separated flows. Originally, Van Driest's[17] function was included in the Baldwin[14] function to eliminate the first maximum (Fig. 2) and the second maximum was then selected as a first maximum of the corrected Baldwin function. The selection of the outermost peak of $F_{\mathrm{Bald}}(y)$ in the length computation can overpredict turbulence scales (Fig. 3). Péchier[12] has recently shown that Van Driest's[17] function alters the second maximum accuracy and has proposed to keep the original Baldwin function and to select the second maximum.

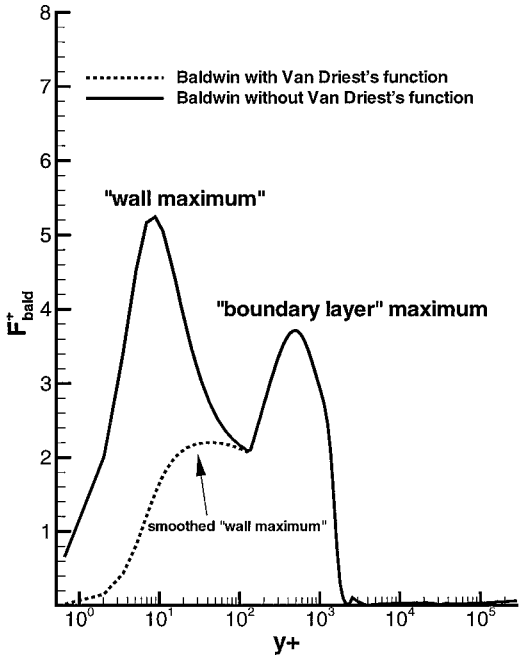

Fig. 2 Baldwin's function behavior for an attached boundary layer.

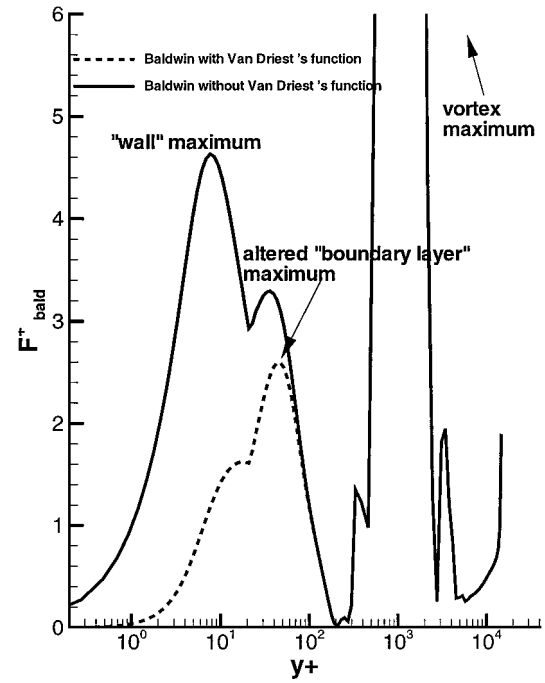

Fig. 3 Baldwin's function behavior in vicinity of separation.

Furthermore, to suppress a slope discontinuity on the μ_t profile at the intersection of inner and outer regions, a smoothing formulation has been introduced:

$$\mu_t = \mu_{te} th(\mu_{ti}/\mu_{te}) \tag{20}$$

Region 2

The Goldberg backflow model[15] has been designed especially for (and is restricted to) separated flow regions. Consequently, it must be combined with another model (region 3). The model is based on experimental observation of separated turbulent flows. The main features of the model are 1) the length scale within the backflow, which is proportional to the local distance from the wall to the edge of the viscous sublayer located outside the backflow region, and 2) the turbulent kinetic energy k and its dissipation ε, which are prescribed analytically in the separation bubble.

Gaussian distribution of turbulent kinetic energy k in the wall-normal direction is assumed between the wall and the edge of the separation bubble y_b:

$$\frac{\rho k}{\rho k_b} = \frac{e^{\varphi}\left\{1 - \exp\left[-\varphi(y/y_b)^2\right]\right\}}{e^{\varphi} - 1} = G(x, y)$$

$$0 \le y \le y_b \tag{21}$$

The dissipation is given by

$$\varepsilon(\rho/\rho_b)^{\frac{3}{2}} = [k_v G(x, y)]^{\frac{3}{2}} \Big/ y_v, \qquad 0 \le y \le y_b \tag{22}$$

The value of k at the viscous sublayer edge y_v follows from

$$\beta \equiv k_v/k_b = 1 + \frac{\left[(y_v/y_b)^2 - 1\right]\varphi}{e^{\varphi} - 1} \tag{23}$$

where

$$y_v/y_b = 1 + 20[\nu_w/u_s y_b]C_\mu^{\frac{1}{4}} \tag{24}$$

where u_s is the square root of the maximum Reynolds shear stress in the profile. This maximum is found outside the separation (region 3) and can be obtained from

$$u_s = \sqrt{-(\overline{u'v'})_{\max}} \tag{25}$$

In the present computations u_s was chosen as

$$u_s = \sqrt{\nu_{t,m}\|\tilde{\Omega}\|_{\max}} \tag{26}$$

where $\nu_{t,m}$ is the eddy viscosity at the location where $\|\tilde{\Omega}\|$ reaches its maximum (outside the separation bubble).

Finally, the eddy viscosity is assumed to be of the following form:

$$\nu_t = f(y/y_b)(k^2/\varepsilon) \tag{27}$$

which gives

$$\nu_t = u_s y_v \sqrt{(\rho_w/\rho)}\sqrt{G(x,y)}[A(y/y_b) + B]\left(1\Big/2\sqrt{2}\beta^2\right) \tag{28}$$

where A and B are given by

$$A = -\left(\tfrac{1}{2}C_\mu^*\right)^{\frac{9}{5}}, \qquad B = \left(\tfrac{1}{2}C_\mu^*\right)^{\frac{3}{5}} - A \tag{29}$$

with the constants

$$C_\mu = 0.09, \qquad C_\mu^* = 0.7, \qquad \varphi = 0.5 \tag{30}$$

Region 3 ($y > y_b$)

The expression of the eddy viscosity in region 3 is given by

$$\mu_t = \bar{\rho}kC_{cp}\tilde{L}\tilde{V}\cdot\tilde{\gamma}[(y - y_b)/(y_{\max} - y_b)] \tag{31}$$

where $\tilde{L} = y_{\max} - y_b$ and $y_{\max}$ is the location where the velocity scale function $\tilde{F}$ defined next reaches its maximum (mixing layer):

$$\tilde{F} = (y - y_b)\|\tilde{\Omega}\| \tag{32}$$

Finally, the velocity scale is given by

$$\tilde{V} = \min\left[\tilde{F}_{\max}, C_w\left(\Delta\tilde{u}^2\Big/\tilde{F}_{\max}\right)\right] \tag{33}$$

where $\Delta\tilde{u}$ is the difference between the local maximum and minimum velocity magnitude for $y > y_b$. C_w is a constant taken equal to 0.75. $\tilde{F}_{\max}$ is the local maximum of $\tilde{F}$ in the region corresponding to $y > y_b$. Turbulence decrease is taken into account by the function

$$\tilde{\gamma}\left(\frac{y - y_b}{y_{\max} - y_b}\right) = \frac{1}{1 + 5.5\{\alpha[(y - y_b)/(y_{\max} - y_b)]\}^6} \tag{34}$$

This function is an adaptation of the Klebanoff intermittence factor formulation. The value of α corresponding to C_{Kleb} in Eq. (22) was chosen equal to 0.8 to predict correctly the mixing layer thickness. This approach differs from the one proposed by Ramakrishnan and Goldberg[19] on the following points: discontinuity smoothing between the internal and external zones, pressure gradient influence in the attached region, turbulent scales evaluation and turbulence decrease formulation in the mixing layer.

Results and Discussion

Grids

To evaluate the accuracy of the different simulations, three grids have been built. They have been obtained by rotating a two-dimensional grid around the nozzle axis. Each grid is divided into two domains. The first one is used to mesh the nozzle, and the second one concerns the external region after the exhaust. The density of the different grids is indicated in Table 1.

The i direction corresponds to the axial flow direction. The j direction is the radial one normal to the axis and k represents the different planes around the nozzle axis. Grid A constitutes the reference grid with which most of the simulations have been performed. Grid B enables one to see the effect of a grid refinement in the radial direction. Grid C allows one to evaluate the influence of the number of radial planes (one every 5 deg instead of one every 10 deg in the reference grid A).

Table 1 Grid size characteristics

Location	Grid A	Grid B	Grid C
Nozzle ($i \times j \times k$)	$161 \times 100 \times 37$	$239 \times 150 \times 37$	$161 \times 100 \times 73$
Exterior ($i \times j \times k$)	$100 \times 180 \times 37$	$121 \times 200 \times 37$	$100 \times 180 \times 73$
Total (nodes)	≈1,300,000	≈2,200,000	≈2,500,000

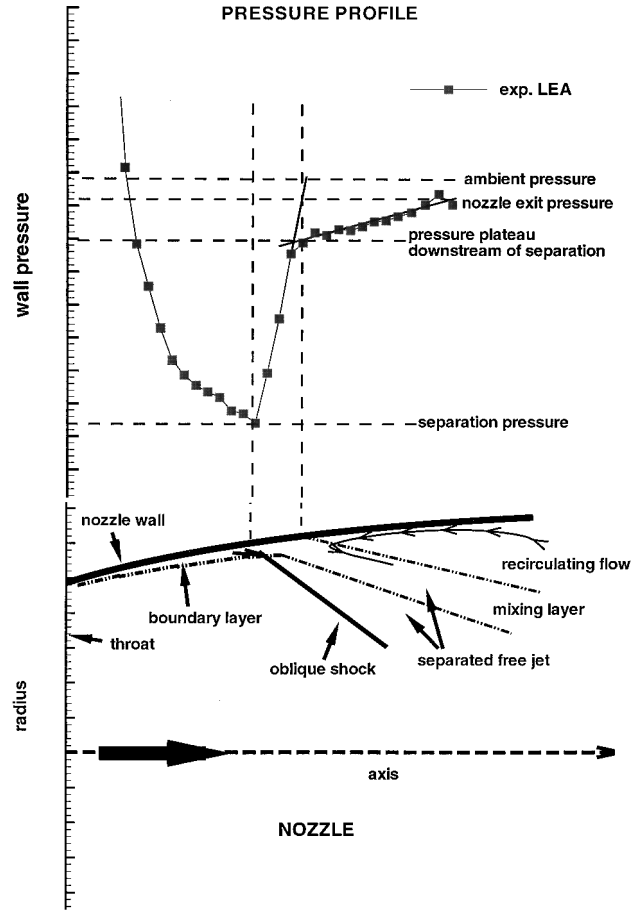

Fig. 4 Free-shock separation–wall pressure behavior.

Computation Description

A wide range of pressure ratios has been simulated, from 30, where the separation occurs near the throat, to 85, where the separation is located near the nozzle exit. Computations were carried out on a NEC SX-5 supercomputer. The CPU cost per cell and per iteration is 1.2 μs. Computations are carried out in two steps. First, a steady computation is performed to fix the shock position. Then the unsteady computation begins.

Flowfield Description

The separated flowfield description is presented in Fig. 4, along with the wall pressure distribution. Separation and subsequent formation of a recirculation zone induce an oblique shock wave near the wall. This oblique shock results in a wall pressure rise. Aft of the separation, the wall pressure reaches a plateau. Downstream of this plateau, the wall pressure increases slowly up to the ambient pressure. This overexpanded flow pattern is called free-shock separation.[7]

Figure 5 shows the streamlines inside the nozzle featuring the free-shock separation phenomenon. The separated flow continues as a freejet. Consequently, a large part of the extension is filled by the ambient gas. The outer fluid is sucked into the nozzle; it separates from the nozzle lip and reattaches at the nozzle wall to form a clockwise recirculating bubble.

Figures 6a and 6b give the typical pressure and Mach contours of the flowfield inside the nozzle featuring the free-shock separation

phenomenon. The flow separates and does not reattach. The conical shock propagating toward the nozzle axis may have two different shock patterns according to the pressure ratio. In the first case, corresponding to a pressure ratio (PR) of 50, a strong Mach disk is obtained (Fig. 6a), whereas in the second case (Fig. 6b for PR = 85), the conical shock reaches the axis (in an axisymmetric flowfield, a small Mach disk should theoretically exist). The exhaust jet flow is delimited by a mixing layer through a channel. The mixing layer can be considered as a fluid wall in which the supersonic jet is confined.

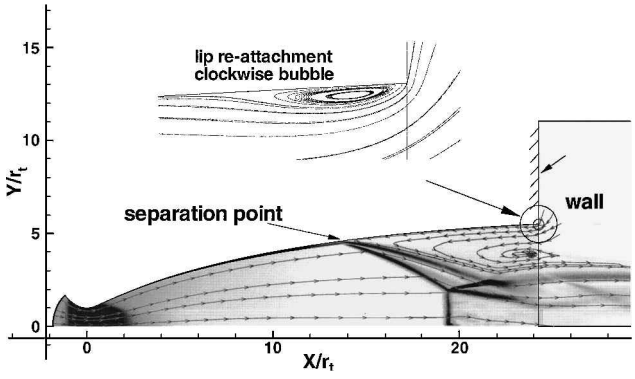

Fig. 5 Flowfield description.

Grid Convergence

To evaluate the effect of grid refinement, two computations were carried out on grids B and C for a PR of 50. Figure 7 shows a comparison of the results obtained on grids A and B, knowing that no visible difference between grids A and C can be seen. The results are quite close, one can only notice a slight difference on the Mach disk position. Figure 8 presents the value $y+$ at the first mesh point above the solid surface of grid A for the same PR. Its value always stays below 1.1, which is quite sufficient for a correct calculation of the viscous stresses.

Pressure Distribution

Downstream of the separation shock, the flow does not remain uniform. The separation has an unsteady and three-dimensional behavior, which leads to nonsymmetrical pressure loads on the wall, discussed in more detail later. The overall wall pressure data for different azimuthal positions are compared in Fig. 9. The mean steady wall pressure obtained during the Laboratoires d'Études Aérodynamiques (Poitiers, France) (LEA) experiments (symbol) have been plotted together with the instantaneous wall pressure obtained numerically (solid line). The different curves correspond to

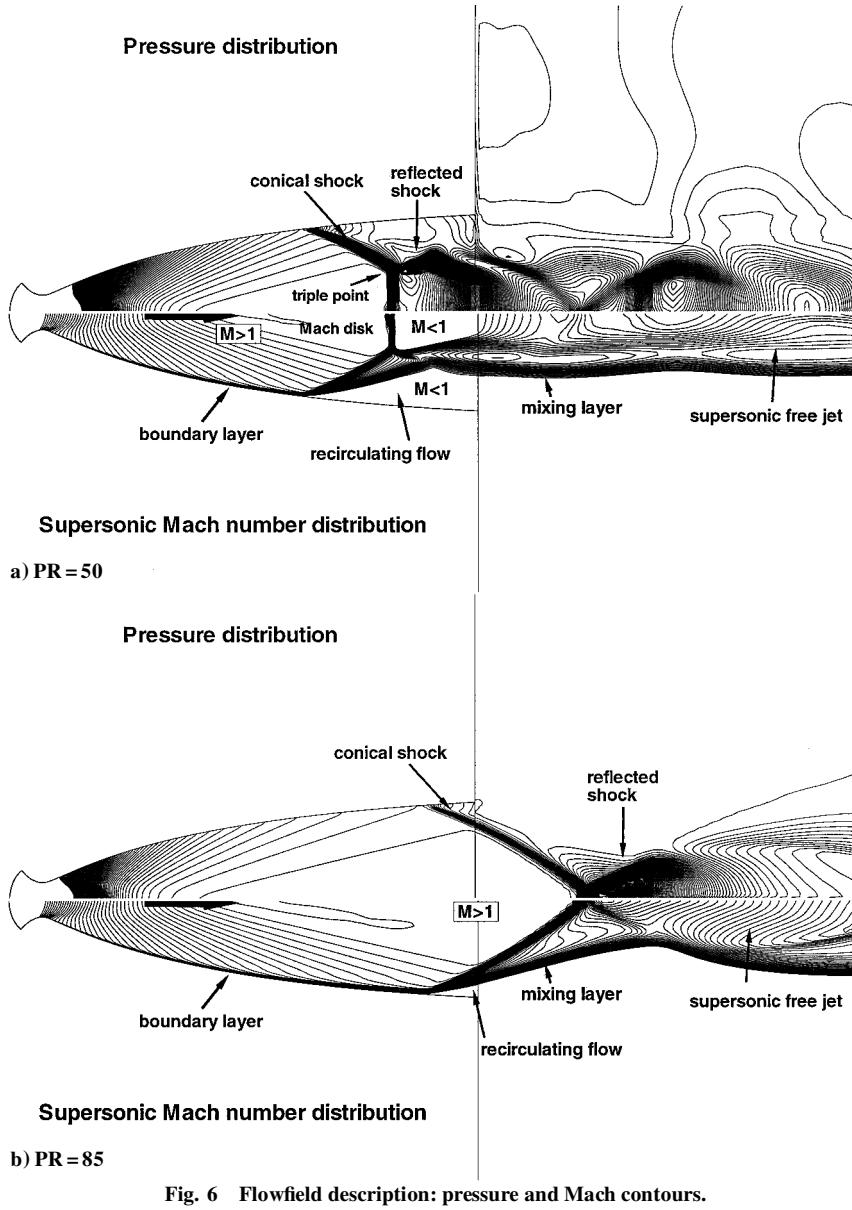

Fig. 6 Flowfield description: pressure and Mach contours.

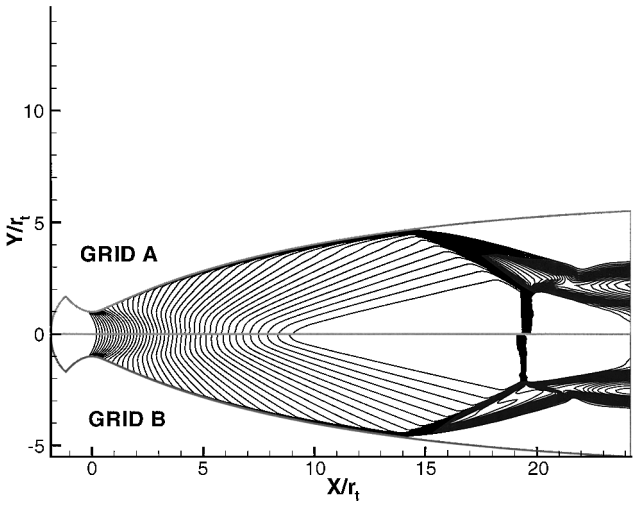

Fig. 7 Effect of grid resolution on Mach contours for grids A and B.

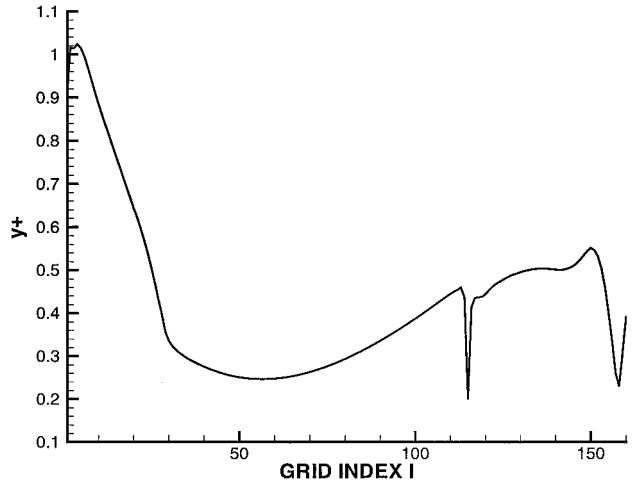

Fig. 8 Value *y*+ size of neighboring wall cells (PR = 50).

a meridian line around the nozzle. The discrepancies between these curves demonstrate the nonaxisymmetric nature of the flowfield. The pressure obtained downstream of the separation point is irregular.

Separation Prediction

Many authors[20–26] have developed purely empirical correlations to determine the separation point location. A brief review of these criteria can be found in Ref. 27. Figure 10 shows the position of the separation point with respect to the PR according to the different criteria, the experimental results, and our computations. Note that the location of the separation point is clearly underestimated with all of the empirical criteria for high PRs, whereas the computations are in good agreement with the experimental data. More precisely, the computed separation point location differs by less than 5% from experimental data.

Side-Loads Prediction

Side loads have been observed both in subscale and full-scale nozzles during transient operations such as startup or shutdown, as well as during steady operation with separated flow inside the nozzle. In general, flow separation leads to lateral forces, that is, side loads due to an asymmetrical pressure acting on the nozzle wall. The potential origins of these aerodynamic side loads found in the literature are 1) external flow instabilities, buffeting (not considered in this discussion), 2) aeroelastic coupling of separation and nozzle extension, 3) transition of separation pattern from free-shock separation to restricted-shock separation and vice versa, and 4) random pressure pulsations at the separation point and in the whole separated flow region. The nozzle considered here is a truncated ideal contoured nozzle where free shocks do not reattach. This nozzle is rigid to separate aeroelastic from aerodynamic phenomena. Furthermore, this kind of nozzle does not produce an internal shock, which could lead to a cap-shock pattern. Consequently, the aforementioned second and third points can be dropped in the following discussion. Furthermore, side loads have been observed for both cold and hot gases.[7] As a consequence, combustion and hot-gas effects are excluded in the present work as a dominating source of lateral forces.

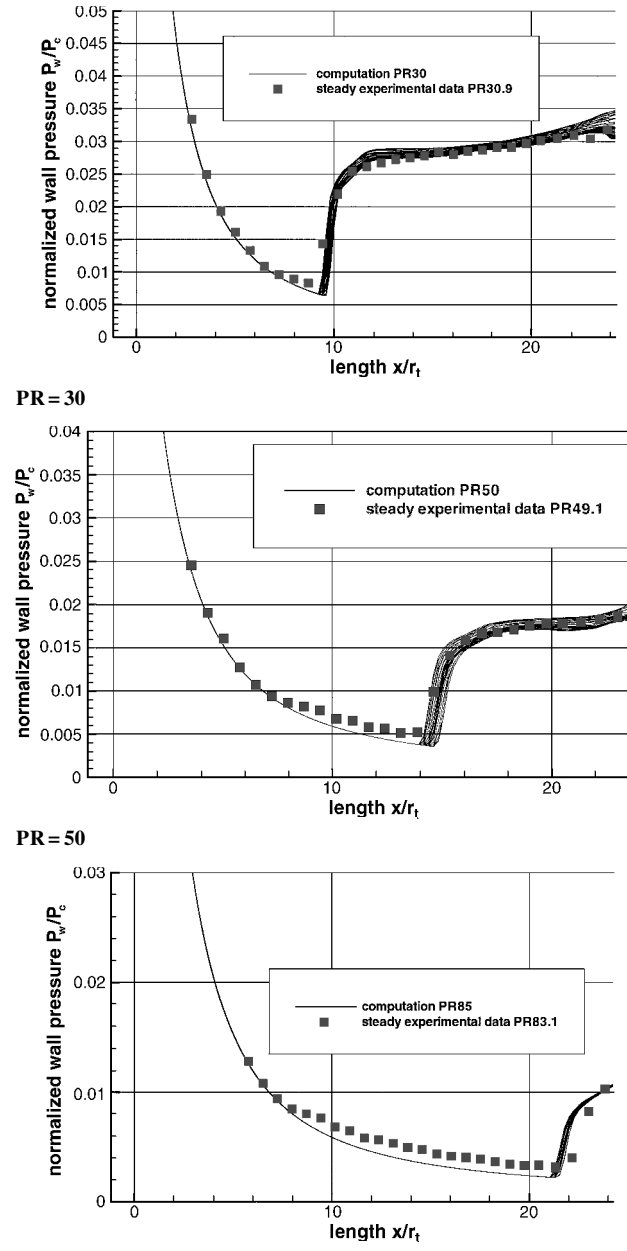

Fig. 9 Instantaneous wall pressure distribution.

Figure 11 gives a schematic view of the evolution of the separation line and introduces the two parameters $[\theta(t), F(t)]$ used to qualify the side load. Here $\theta(t)$ is the angle between the instantaneous side force and a reference axis. $F(t)$ is the instantaneous side-force norm.

Figure 12 shows the evolution of the pressure effort $F(t)$ for a PR equal to 50 during 1.1 s. Figure 13 shows the evolution of the side-force vector direction $(\cos(\theta(t)), \sin(\theta(t))$ as a function of time (z axis). This load has a random direction. The large-amplitude and low-frequency side-load fluctuations are induced by the flow unsteadiness.

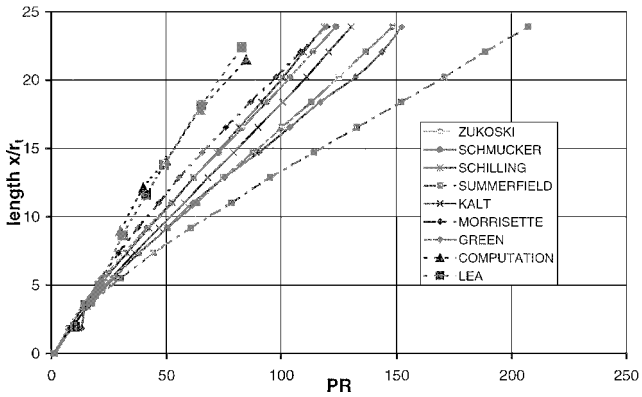

Fig. 10 Prediction of the separation point location with different criteria.

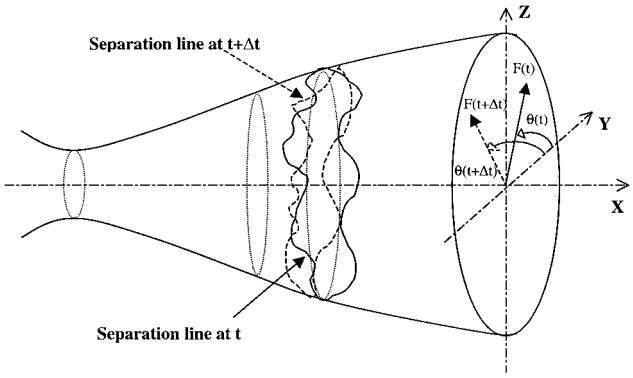

Fig. 11 Definition scheme of the parameters $[\theta(t), F(t)]$.

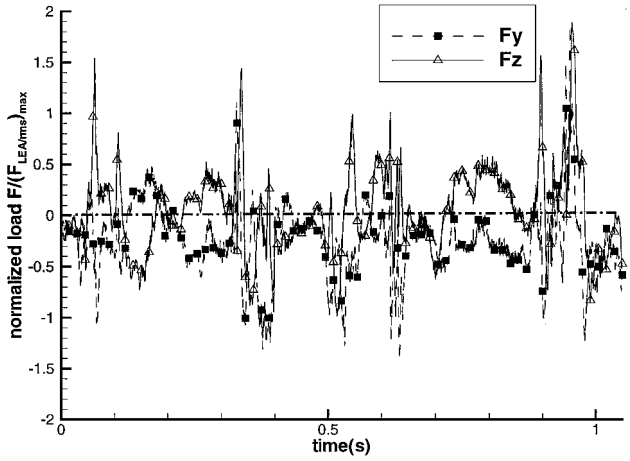

Fig. 12 Time history of y and z components of the fluctuating side loads.

In connection with these considerations, it is interesting to take into account the probability density function of the side loads. The probability density function of given physical data describes the probability that the data assume a value within a prescribed range at any instant. Comparison of the side-force probability density obtained by our unsteady turbulent computation with experimental results obtained by LEA is given in Fig. 14. Both indicate that the distribution of the side-load amplitude is a Rayleigh distribution, as suggested by Dumnov.[28] The Rayleigh probability distribution function is described with the following formulas:

$$P(x \mid c) = (x/c^2)\exp(x^2/2c^2), \qquad x \geq 0, \qquad \text{otherwise zero} \tag{35}$$

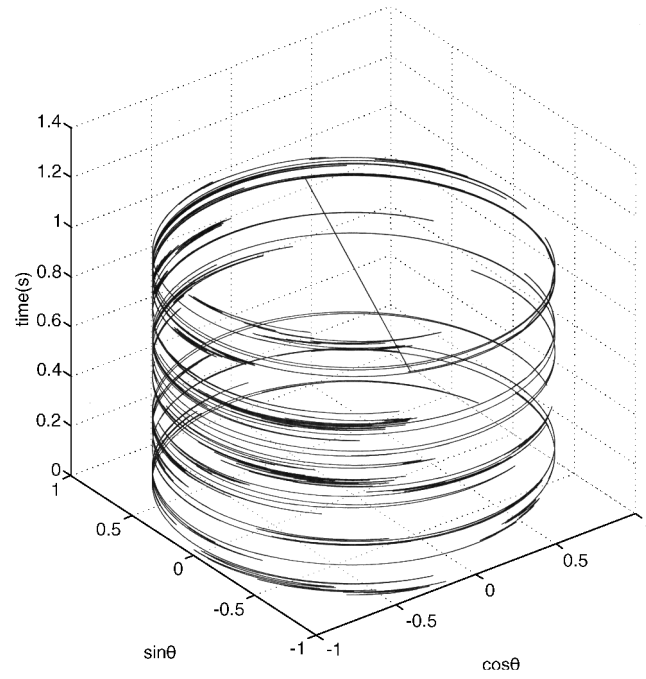

Fig. 13 Time history of side-loads direction.

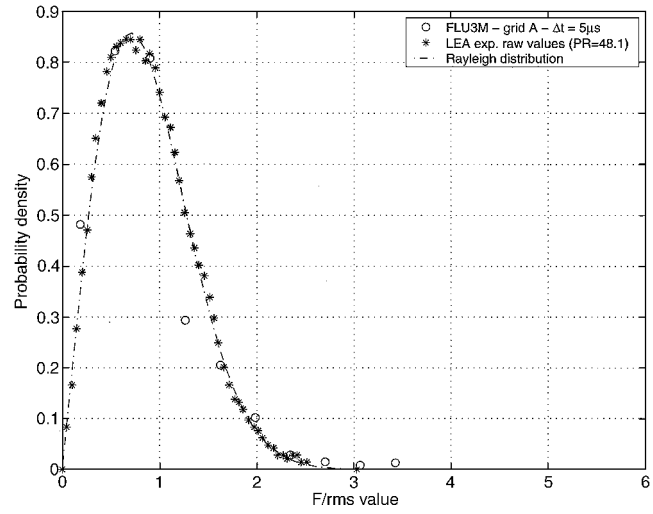

Fig. 14 Probability density function of side-load amplitude distribution.

The most likelihood estimator (MLE) used is

$$c = \sqrt{\frac{1}{2n}\sum_{i=1}^{n} x_i^2}$$

where x is the random value of the amplitude and n is the size of the sample.

As a classical result of data signal processing, this suggests that the components of the side loads in the y and z directions are two independent normal random variables with zero mean and equal variance.

Time and Grid Convergence

To see the effect of the time step on the side-load prediction, calculations have been performed with different grids and time steps for a PR of 50. The results of these tests are summarized in Table 2.

If the grid C (finest grid) with the smallest time step is considered as a reference, we obtain a converged result with the couple (grid A, $\Delta t = 10$ μs). This couple (less costly) is then retained for the following computations.

Table 2 Time and grid convergence

Grid	Δt, μs	Side load rms
A	200	0.67
A	50	0.61
A	10	0.74
C	5	0.73

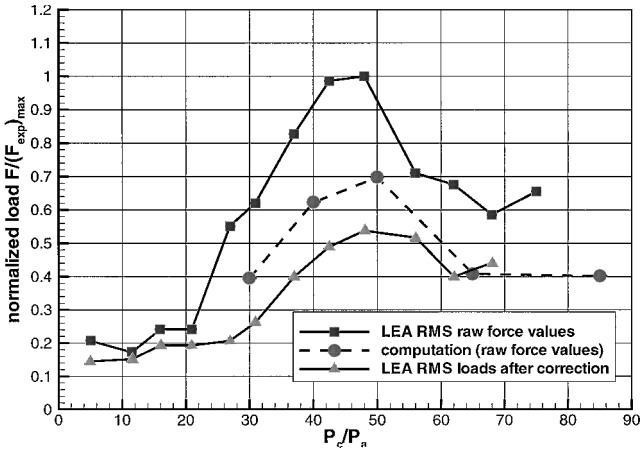

Fig. 15 LEA rms side-load evolution.

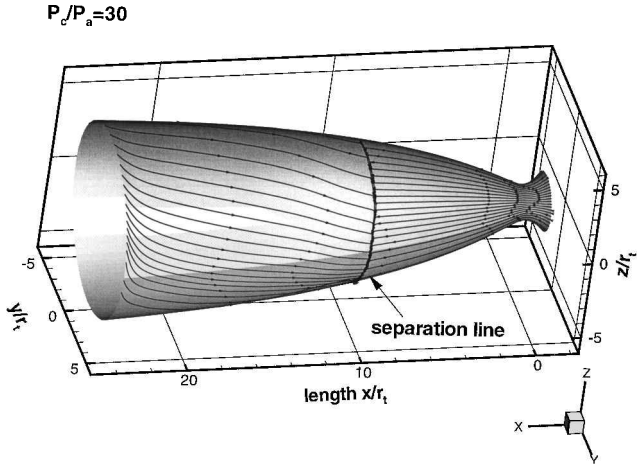

Fig. 16 Skin-friction lines (PR = 30).

Figure 15 compares the experimental rms value of the side load obtained by LEA with the computed values for different PRs. Two experimental curves are given by LEA. The first one corresponding to the highest level represents the forces directly measured on the nozzle by mean of sensors, which includes both the loads due to the aerodynamics and those due to the coupling between aerodynamics and structures. The evaluation of the aerodynamic forces alone requires some very delicate corrections.[10] The second experimental curve showing a lower level corresponds to these corrected values. The numerical results fall within the two experimental curves, which can be considered as satisfactory knowing the difficulty of the experimental evaluation. Both values indicate that the maximum is reached for a PR around 50, that is, when the separation point is located in the middle of the nozzle extension.

The calculations have revealed two main features of the separated flow: first, the unsymmetrical separation and, second, the pressure pulsation that emanates from the separation point. It results in unsymmetrical wall pressure distributions.

Once the separation occurs, the flow loses its axisymmetrical nature. This leads to pressure pulsations and to separated flow unsteadiness. The loss of the axisymmetrical nature is illustrated by plotting the skin-friction lines (Fig. 16).

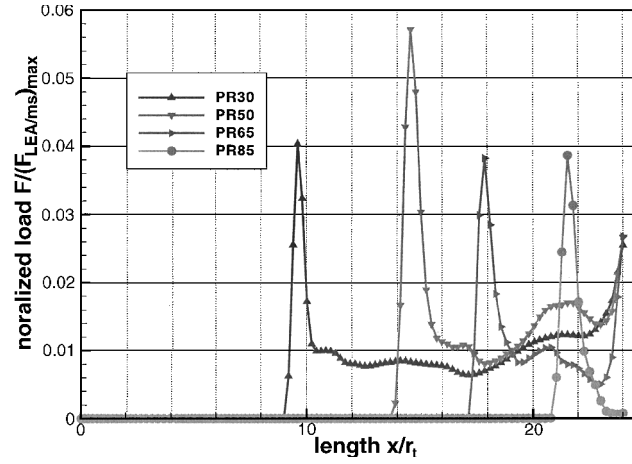

Fig. 17 Local side-load contribution.

Unsteady and unsymmetrical behavior in the subsonic recirculating flow influences the position of the separation line. This behavior seems to be important when the separation shock emanates in a region of minor wall curvature.

Figure 17 presents the absolute value of the local side load $\partial|F|/\partial x$ with respect to x for the different PRs computed (at a given time), respectively. Two important contributions are observed for a chosen PR. The first one comes from the separation and is characterized by the peak in Fig. 17. This peak is related to the nonaxisymmetrical behavior of the separation line. The second one originates from the region located downstream of this peak and exhibits a plateau showing that some small pressure fluctuations can contribute to nonnegligible sideloads.

Conclusions

This study has shown the interest of an algebraic model based on Goldberg's[15] backflow formulation to predict the free-shock separation pattern in a wide range of PRs.

The computed nozzle wall pressures are in good agreement with the experimental measurements. More precisely, the separation point location differs from experimental data by less than 5%, and the plateau pressure level downstream of the separation is accurately predicted. From this point of view, it improves significantly on semi-empirical prediction tools.

Moreover, both the three-dimensional and unsteady behavior were simulated. The analysis of the flowfield suggests that the unsteadiness is strictly located downstream of the separation shock. The numerical flow remains perfectly axisymmetric upstream.

The side-loads prediction, as well as the random characteristics, also are in good agreement with the available experimental data, particularly the global behavior of the rms force evolution vs the PR that have been well reproduced. Probability density of side-load distribution follows Rayleigh's law. The numerical study revealed two main side-load features in the LEA truncated ideal contoured nozzle. The large-amplitude and low-frequency side-loads fluctuation are induced by the flow unsteadiness. Downstream of the separation point, the flow is not axisymmetric in space. The turbulent shear layer that emanates from the separation point causes pressure pulsations in the whole separated flow region. The numerical study indicates finally that small pressure pulsations are sufficient to generate non-negligible loads on the nozzle wall.

Acknowledgments

This study, as well as the thesis grant of the first author, is partly funded by the Centre National d'Etudes Spatiales (CNES) within the framework of the CNES Research and Technology Program ATAC (aerodynamics of nozzle and afterbodies) under technical cooperation between CNES/ONERA/Centre National de la Recherche Scientifique/SNECMA and EADS-LV. The authors are greatly indebted to Alziary and Girard from the Laboratoires d'Études Spatiales for supplying the experimental data and the initial mesh and to their

colleagues, Péchier, Champigny, Duveau, Garnier, and Hallard, for fruitful discussions.

References

[1]Haguemann, G., and Reijasse, P., "Brief Review of Side-Load Models," DLR-IB 645-98136; also published as Rept. ONERA RT 44/4361 DAFE/Y, Lampoldhausen, Dec. 1998.

[2]Chen, C. L., Chakravarthy, S. R., and Hung, C. M., "Numerical Investigation of Separated Nozzle Flows," *AIAA Journal*, Vol. 32, No. 9, 1994, pp. 1836–1843.

[3]Onofri, M., Nasuti, F., and Bongiorno, M., "Shock Generated Vortices and Pressure Fluctuations in Propulsive Nozzles," AIAA Paper 98-0777, June 1998.

[4]Onofri, M., and Nasuti, F., "The Physical Origins of Side Loads in Rocket Nozzles," AIAA Paper 99-2587, June 1999.

[5]Ostlund, J., "Assesment of Turbulence Models in Overexpanded Rocket Nozzle Flow Simulations," AIAA Paper 99-2583, June 1999.

[6]Frey, M., and Haguemann, G., "Flow Separation and Side-Loads in Rocket Nozzles," AIAA Paper 99-2815, June 1999.

[7]Frey, M., and Haguemann, G., "Status of Flow Separation Prediction in Rocket Nozzles," AIAA Paper 98-3619, June 1998.

[8]Terhardt, M., and Haguemann, G., "Flow Separation and Side-Load Behavior of the Vulcain Engine," AIAA Paper 99-2762, June 1999.

[9]Östlund, J., and Bigert, M., "A Sub Scale Investigation on Side Loads in Sea Level Rocket Nozzles," AIAA Paper 99-2759, June 1999.

[10]Girard, S., and Alziary de Roquefort, T., "Etude des charges latérales dans les tuyères. Rapport d'exploitations d'essais," LEA Unité de Recherche Appliquée CNRS 191, Dec. 1996.

[11]Péchier, M., Guillen, Ph., and Caysac, R., "Magnus Effect over Finned Projectiles," *Journal of Spacecraft and Rockets*, Vol. 38, No. 4, 2001, pp. 542–549.

[12]Péchier, M., "Previsions numériques de l'effet Magnus pour des configurations de munition," Ph.D. Dissertation, Dept. of Mechanical Engineering, Univ. of Poitiers, Poitiers, France, Sept. 1999.

[13]Visbal, M., and Knight, D., "The Baldwin Lomax Turbulence Model for Two-Dimensional Shock-Wave/Boundary-Layer Interactions," *AIAA Journal*, Vol. 22, No. 7, 1984, pp. 921–928.

[14]Baldwin, B. S., and Lomax, H., "Thin Layer Approximation of Algebraic Model for Separated Turbulent Flows," AIAA Paper 78-0257, Jan. 1978.

[15]Goldberg, U. C., "Separated Flow Treatment with a New Turbulence Model," *AIAA Journal*, Vol. 24, No. 10, 1986, pp. 1711–1713.

[16]Cebeci, T., and Smith, A. M. O., "Analysis of Turbulent Boundary Layers," Applied Mathematics and Mechanics, Academic Press, New York, 1974.

[17]Van Driest, E. R., "On Turbulent Flow Near a Wall," *Journal of the Aeronautical Science*, Vol. 23, Nov. 1956, pp. 1007–1036.

[18]Piquet, J., "Turbulent Flows-Model and Physics," Springer, 1999, pp. 471–495.

[19]Ramakrishnan, S., and Goldberg, U. C., "Numerical Simulation of Swept Shock/Boundary-Layer Interactions," AIAA Paper 90-5234, Oct. 1990.

[20]Zukoski, E. E., "Turbulent Boundary Layer Separation in Front of a Forward Facing Step," *AIAA Journal*, Vol. 5, No. 2, 1967, pp. 1746–1753.

[21]Schumcker, R. H., "Status of Flow Separation Prediction in Liquid Propellant Rocket Nozzles," NASA, TM X-64890, Nov. 1974.

[22]Schilling, M. T., "Flow Separation in Rocket Nozzles," Ph.D. Dissertation, Univ. of Buffalo, Buffalo, June 1962.

[23]Summerfield, M., Foster, C., and Swan, W., "Flow Separation in Overexpanded Supersonic Exhaust Nozzles," *ARS Journal*, Vol. 24, No. 5, 1954, pp. 319, 320.

[24]Kalt, S., and Bendal, D., "Conical Rocket Nozzles Performance Under Flow Separated Conditions," *Journal of Spacecraft and Rockets*, Vol. 2, No. 3, 1965, pp. 447–449.

[25]Morisette, E. L., and Goldberg, T. J., "Turbulent Flow Separation Criteria for Overexpanded Supersonic Nozzles," NASA, TP-1207, 1978.

[26]Green, L., "Flow Separation in Rocket Nozzles," *ARS Journal*, Vol. 23, No. 1, 1953, pp. 34, 35.

[27]Aupoix, B., Casalis, G., Regard, D., Reijasse, Ph., and Veuillot, J. P., "Etude des phénomènes de décollement et des efforts latéraux dans les tuyères surdétendues," Rapport intermédiaire, DERAT 645005.70, Sept. 1994.

[28]Dumnov, G. E., "Unsteady Side Loads Acting on the Nozzle with Developed Separation Zone," AIAA Paper 96-3220, June 1996.